JACS
JOURNAL OF THE AMERICAN CHEMICAL SOCIETY
Article
Cite This: J. Am. Chem. Soc. 2018, 140, 7239−7247
pubs.acs.org/JACS

Internal Electric Field Modulation in Molecular Electronic Devices by Atmosphere and Mobile Ions

Prakash Chandra Mondal,[†] Ushula M. Tefashe,[†] and Richard L. McCreery*

Department of Chemistry, University of Alberta, Edmonton, Alberta T6G 2G2, Canada

Supporting Information

ABSTRACT: The internal potential profile and electric field are major factors controlling the electronic behavior of molecular electronic junctions consisting of ∼1−10 nm thick layers of molecules oriented in parallel between conducting contacts. The potential profile is assumed linear in the simplest cases, but can be affected by internal dipoles, charge polarization, and electronic coupling between the contacts and the molecular layer. Electrochemical processes in solutions or the solid state are entirely dependent on modification of the electric field by electrolyte ions, which screen the electrodes and form the ionic double layers that are fundamental to electrode kinetics and widespread applications. The current report investigates the effects of mobile ions on nominally solid-state molecular junctions containing aromatic molecules covalently bonded between flat, conducting carbon surfaces, focusing on changes in device conductance when ions are introduced into an otherwise conventional junction design. Small changes in conductance were observed when a polar molecule, acetonitrile, was present in the junction, and a large decrease of conductance was observed when both acetonitrile (ACN) and lithium ions (Li^+) were present. Transient experiments revealed that conductance changes occur on a microsecond−millisecond time scale, and are accompanied by significant alteration of device impedance and temperature dependence. A single molecular junction containing lithium benzoate could be reversibly transformed from symmetric current−voltage behavior to a rectifier by repetitive bias scans. The results are consistent with field-induced reorientation of acetonitrile molecules and Li^+ ion motion, which screen the electrodes and modify the internal potential profile and provide a potentially useful means to dynamically alter junction electronic behavior.

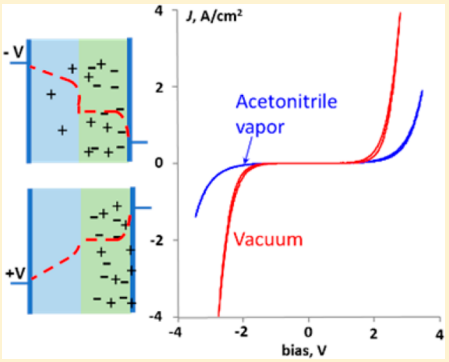

INTRODUCTION

The field of molecular electronics (ME) seeks to realize novel electronic functions with molecules as active circuit elements, often in "molecular junctions" (MJs) composed of single molecules or nanometric (1−20 nm) thick molecular layers between conducting contacts. Of particular interest are electronic functions that are difficult or impossible to achieve with conventional semiconductors, often with special requirements such as flexibility, low power consumption, less heat generation or very low manufacturing cost. Redox reactions and motion of ions are phenomena that are rarely involved or are deleterious in conventional microelectronics, but have been used for various electronic functions in memory,[1−3] rectification,[4,5] light emission,[6−8] and the field of "nanoionics".[9,10] For example, Bard. et al. showed that ion motion was essential for light emission by solid-state devices containing ∼100 nm thick films of a Ru^{2+}-bipyridyl polymer, and that the effect was sensitive to residual water.[11−13] High levels of ions (10^{18}−10^{20} cm^{-3}) added to ∼100 nm organic films were shown to screen the electrodes, reduce the internal electric field, and increase electroluminescent behavior or organic light emitting diodes (OLEDs).[14,15] Electrolyte gated organic thin film transistors also involve ion motion, and show distinct effects of both "electrostatic" and "electrochemical" doping in 30 nm thick organic films.[16,17] Redox reactions and accompanying ion (or vacancy) motion have also been invoked to explain conductance changes in devices containing TiO_2,[18−20] some of which are strongly affected by trace water vapor.[21] More recently, mobile ions have been reported to significantly alter the conductance of molecular junctions, due to redox reactions in Li^+ containing trilayer junctions[22] or by orbital realignment from mobile PF_6^- ions in molecular rectifiers.[5] Solvents and nearby molecules can significant affect single molecule conductance[23−25] through electronic interactions, and atmospheric gases can strongly affect both the current magnitude and attenuation constant for large area molecular junctions using eutectic indium/gallium contacts.[26]

The current investigation was stimulated in part by the observation that atmospheric H_2O significantly modified the conductance of a 13 nm thick layer of a $Ru^{2+}(bpy)_3$ derivative between carbon electrodes, causing strong hysteresis in current−voltage behavior as well as a pronounced scan rate dependence.[27] The remainder of that study was conducted in a vacuum as a result, but the mechanism by which water affects the junction's electronic properties was not determined. Figure 1A shows a schematic diagram for a molecular junction consisting of eight subunits of a fluorene (FL) oligomer

Received: March 23, 2018
Published: May 17, 2018

DOI: 10.1021/jacs.8b03228
J. Am. Chem. Soc. 2018, 140, 7239−7247

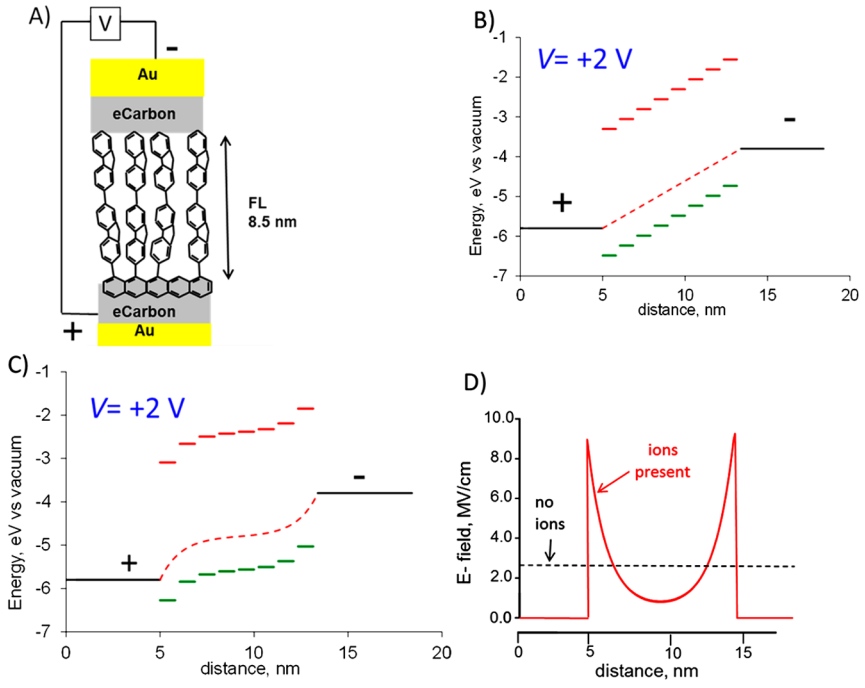

Figure 1. (A) Schematic diagram for Au/eC/$FL_{8.5}$/eC/Au molecular junctions, (B) energy level diagram in the absence of Li^+ ions, (C) when low concentration (0.005 M) mobile ions is present, (D) internal electric field profile (MV/cm) as a function of distance (nm) with and without mobile ions.

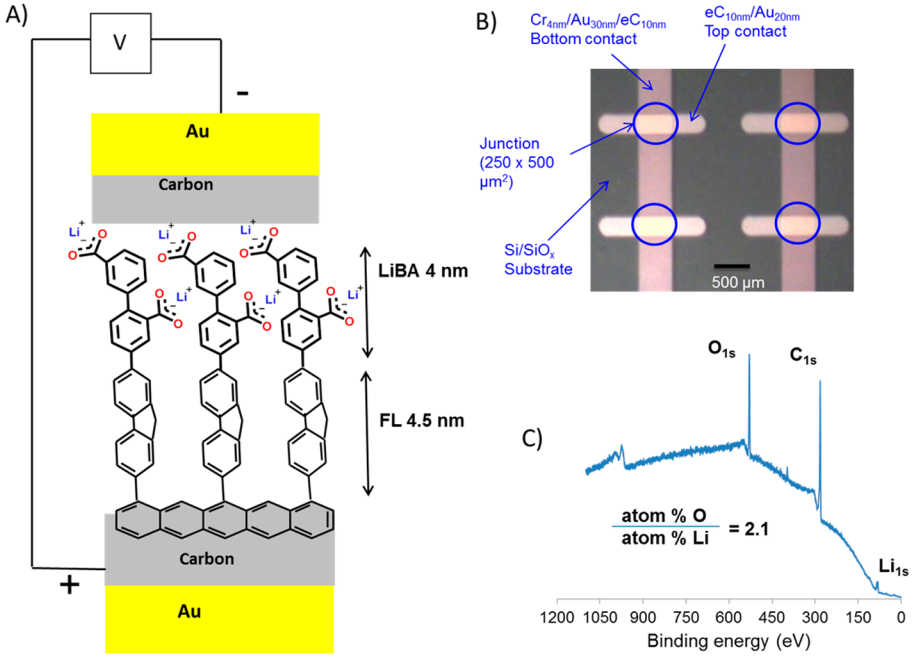

Figure 2. (A) Schematic diagram for Au/eC/$FL_{4.5}$/$LiBA_4$/eC/Au molecular junctions, (B) optical image of four molecular junctions with scale bar. (C) XPS survey spectrum with elemental analysis. Additional XPS spectra and analysis are provided in SI section 5.

between conducting contacts in the absence of mobile ions. Under the common assumption of a linear potential profile, the molecular orbital energies are shifted into a staircase, such as that shown in Figure 1B. The presumed linear profile shown as a dashed red line is modified by electronic interactions with contacts and polarization in real devices,[28−30] but does provide an initial approximation for considering the effects of ions. When mobile ions are present, classical Guoy−Chapman−Stern double layer theory provides guidance about how they affect the internal electric field, although it should be considered approximate given the few-nm dimensions of a molecular junction. Figure 1C shows the effect of a low concentration of mobile ions (0.005 M) of a symmetric electrolyte such as LiF, assuming that the ions are distributed according to Guoy−Chapman−Stern theory. Attraction of the ions to the electrodes partially screens the internal electric field, leading to significant shifts in the potential profile and molecular orbital energies. Note that the highest occupied

DOI: 10.1021/jacs.8b03228
J. Am. Chem. Soc. 2018, 140, 7239−7247

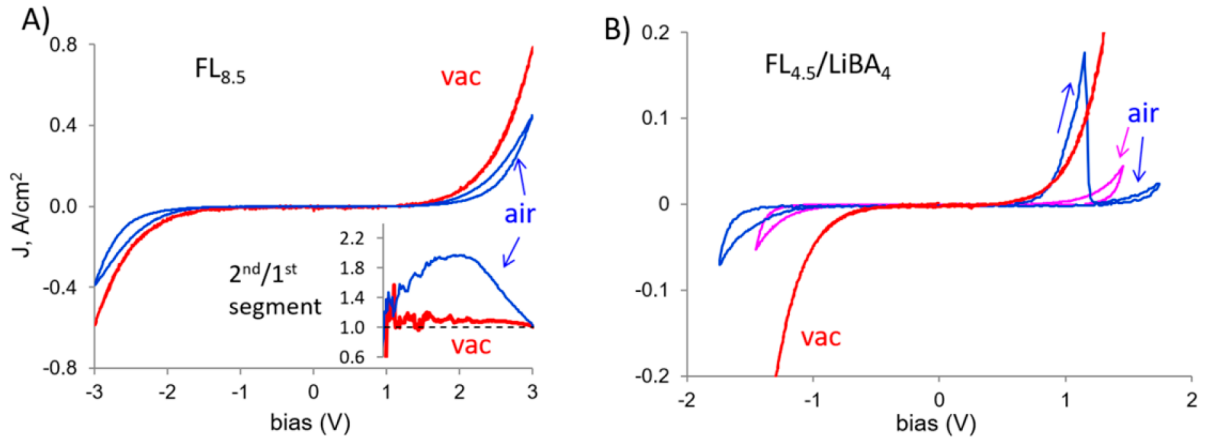

Figure 3. (A) *JV* response of eC/$FL_{8.5}$/eC in a vacuum (red curve) and air (blue curve). Scan rate 1000 V/s, (B) *JV* response of eC/$FL_{4.5}$/$LiBA_4$/eC in a vacuum (red curve), initial scan in air (blue curve) and in air after several scans (pink curve).

molecular orbital (HOMO) level of the second fluorene subunit from the left electrode is now resonant with the Fermi level of the electrode, possibly leading to significantly higher electronic current than the case of Figure 1B. As shown in Figure 1D, the electric field (*E*, MV/cm) with ions present is no longer constant through the device, and has significantly higher magnitude near the electrodes. The importance of the ionic double layer is well-known in electrochemistry, and it underlies most of the widespread applications of heterogeneous electron transfer reactions. The current investigation was undertaken to determine if ion motion can affect the electronic behavior of molecular junctions, with the long-term goal of designing new electronic functions enabled by electrode screening.

As noted above, water vapor can have dramatic effects on molecular junction behavior, but the origin of its effects is complicated by the possibility of water acting as a redox system (for $V > 1$ V), a source of ions, and for solvation of ions intentionally introduced in the molecular layer. The current study started with MJs in a vacuum, initially with no intentional ions present, then with molecules containing lithium benzoate to provide a source of Li^+ ions. Acetonitrile vapor introduced into the vacuum chamber can assist Li^+ motion without being redox active, hence permitting control of ion motion.[22,31] The introduction of ionic groups and mobile ions into molecular junctions is shown to significantly alter electronic behavior without any known involvement of water molecules.

EXPERIMENTAL SECTION

The carbon/molecule/carbon junction fabrication has been described in detail,[27,32] and all devices reported here had the same external device structure, i.e., SiO_x/Cr_4/Au_{30}/eC_{10}/molecules/eC_{10}/Au_{20}, where subscripts indicate layer thicknesses in nm. Electron beam deposited carbon (eC) on both the top and bottom contacts resulted in compositionally symmetric devices, although there may be differences in bonding between the two molecule/eC interfaces. Molecular layers were deposited on Au/eC substrates by electrochemical deposition of diazonium ions made from 2-amino fluorene (FL) and *meta*-amino benzoic acid (BA), in many cases as molecular bilayers.[33] Synthesis, characterization of diazonium salts, substrate preparation, and electrochemical grafting are discussed in the Supporting Information (SI), Schemes S1 and S2, Figures S1–S3, and Table S1. Molecular layer thicknesses were determined by AFM "scratching" and statistical analysis,[33,34] as described in SI section 4, and are rounded to the nearest 0.5 nm (Figure S4). A schematic of the $FL_{4.5}$/$LiBA_4$ bilayer junction made by successive reduction of 2-fluorene diazonium ions is shown in Figure 2A after exchange of the carboxylate proton for Li^+ and top contact deposition, with a photomicrograph of the completed junction in Figure 2B. X-ray photoelectron spectroscopy (XPS) analysis of the $FL_{4.5}$/$LiBA_4$ bilayer without the top contact (Figure 2C) confirms the expected O/Li ratio of 2.1 (Figures S5 and S6, Table S2). Examples of the reproducibility of *JV* responses are shown in Figure S7, with typical relative standard deviations of *J* equal to 10–20%. Electrochemical impedance spectroscopy (EIS) was used to evaluate MJ capacitance, with electrical circuit modeling, Nyquist and Bode plots and corresponding phase plots for $FL_{4.5}$/$LiBA_4$ junctions in a vacuum and ACN vapor discussed in SI section 8 (Figures S8 and S9, Table S3). Additional fabrication and measurement details are provided in SI (Figures S10–15).

RESULTS

The current density (A/cm^2) vs bias (*JV*) response in a vacuum of the fluorene MJ shown in Figure 1A is the red curve of Figure 3A, and is independent of scan rate or repeated scanning. The transport mechanism has been presented previously, and corresponds to multistep tunneling through a barrier defined by the difference in the LUMO and HOMO energies of the fluorene monomer.[28,35] The blue curve in Figure 3A is from the same MJ after exposure to air, exhibiting hysteresis and lower current density, with the current increasing during the scan from +1 to +2 V. This hysteresis is magnified by dividing the current for the second scan segment (+3 to +1 V) by that for the first segment (+1 to +3 V), shown in the inset of Figure 3A. This ratio is 1.0 ± 0.1 in a vacuum, indicating small hysteresis, whereas it exceeds 1.8 ± 0.1 in air. The hysteresis occurs for both polarities, and repeated scanning yields an overall lower *J* with small hysteresis. Figure 3B shows a similar experiment with the $FL_{4.5}$/$LiBA_4$ MJs having a total thickness of 8.5 nm. In a vacuum, the *JV* response shows no hysteresis and is similar to that for $FL_{8.5}$, but the same MJs in air shows erratic and very different *JV* curves, with strong hysteresis and changes in shape during additional scans. Both FL and FL/LiBA junctions showed irregular behavior in air when their thickness (*d*) exceeded 5 nm, so all subsequent report results were acquired in a vacuum or ACN vapor added in a vacuum. As shown in SI Figure S10B, water vapor introduced into the chamber after obtaining *JV* curves for FL/LiBA in a vacuum has similarly strong effects on the response to those in air, indicating that water is the main source of hysteresis in air.

DOI: 10.1021/jacs.8b03228
J. Am. Chem. Soc. 2018, 140, 7239–7247

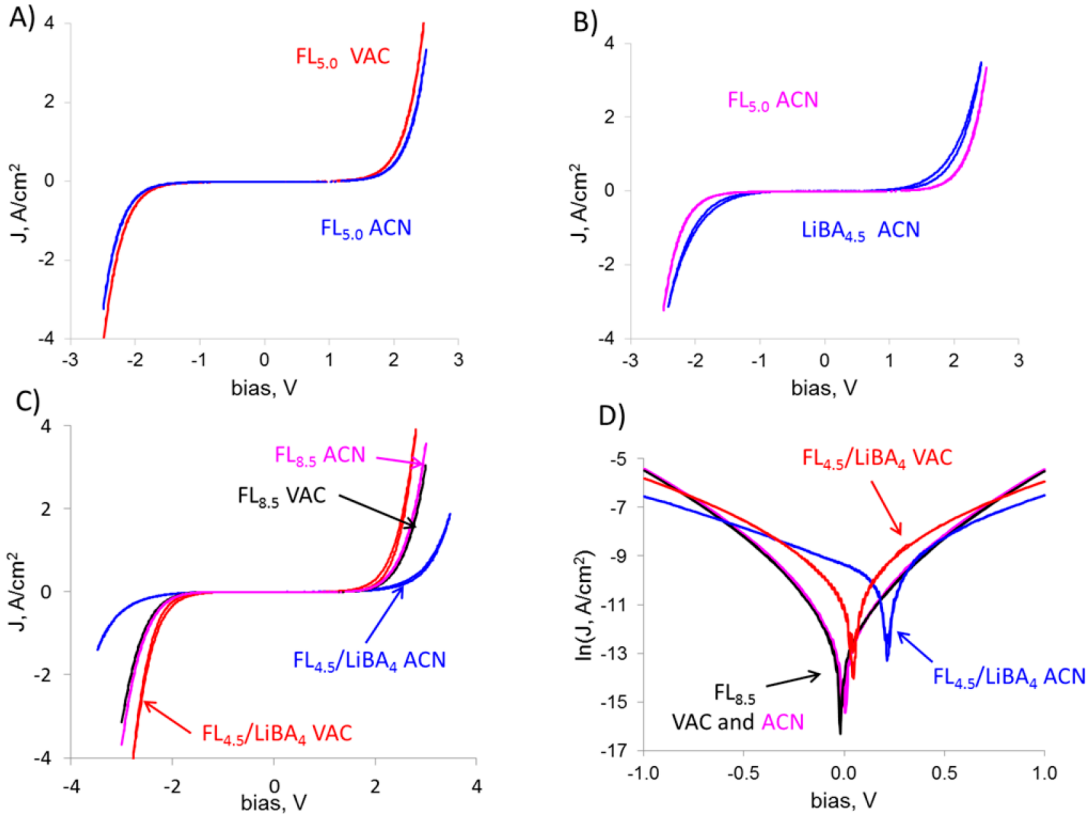

Figure 4. (A) *JV* response of eC/FL_5/eC in a vacuum (red curve) and ACN (blue curve), (B) *JV* response of the same FL junction in ACN (purple curve) and eC/$LiBA_{4.5}$/eC/Au in ACN (blue), (C) *JV* comparison of $FL_{8.5}$ in a vacuum (black), ACN (purple curve), $FL_{4.5}/LiBA_4$ in a vacuum (red curve), and ACN (blue), and D) ln *J* vs bias response of $FL_{8.5}$ in a vacuum (black), ACN (purple), $FL_{4.5}/LiBA_4$ in a vacuum (red), and ACN (blue). *JV* curves are averages of four MJs, with detailed statistics provided in SI Figure S7 and Table S3.

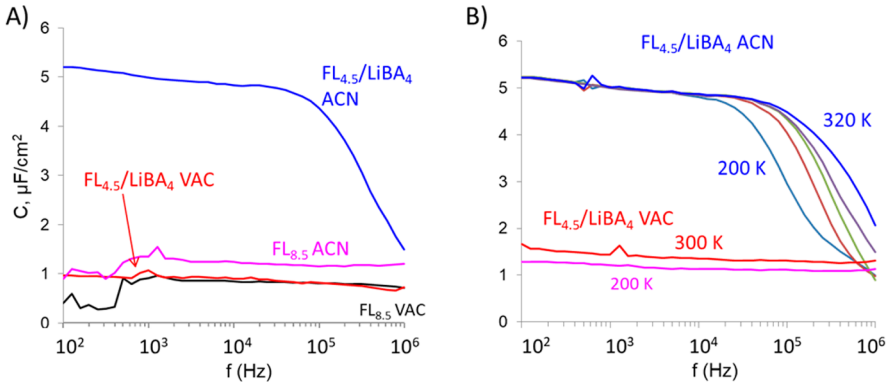

Figure 5. (A) Capacitance of MJs ($\mu F/cm^2$) as a function of frequency (Hz) at 300 K for $FL_{8.5}$ in a vacuum (black), ACN (purple), $FL_{4.5}/LiBA_4$ in a vacuum (red), ACN (blue); (B) temperature dependence capacitance of $FL_{4.5}/LiBA_4$ in a vacuum (purple curve at 200 K, and red curve at 300 K), and in ACN for 200, 240, 280, 300 and 320 K.

Figure 4A shows *JV* curves for a FL_5 MJ with d = 5 nm acquired after exposure to a vacuum (<1 × 10^{-5} Torr) for at least 12 h then again after exposure to ACN vapor for >45 min. ACN vapor causes a small but reproducible decrease in current over the entire *JV* curve. Panel 4B compares JV curves for Fl_5 compared the $LiBA_{4.5}$ in ACN vapor. Although the curves are similar, the LiBA response exhibits hysteresis, with the current increasing in magnitude during the return sweep from either +2.5 or −2.5 V. As shown in SI Table S3, FL and LiBA devices with d = 4.5−5 nm exhibit small but reproducible decreases of 10−15% in *J* when they are exposed to ACN vapor. The effect of ACN may be reduced significantly by strong coupling to the electrodes previously observed for MJs with d < 5 nm.[34] It was not possible to make LiBA junctions thicker than 4.5 nm by electrochemical diazonium reduction, but the effect of ACN exposure on the $FL_{4.5}/LiBA_4$ bilayer was examined, as shown in Figure 4C. For the 8.5 nm thick FL device, ACN exposure has a small effect, with a consistent reduction in the current density of ∼15% in ACN vapor compared to in a vacuum. The mobile ion containing bilayer exhibits a much larger effect of ACN vapor, with *J* decreasing by ∼90%, and with hysteresis observed in either a vacuum or ACN. All *JV* curves in figures were obtained in a vacuum with a scan rate of 1000 V/s, and each curve presented in figures is an average of at least four MJs. The

DOI: 10.1021/jacs.8b03228
J. Am. Chem. Soc. 2018, 140, 7239−7247

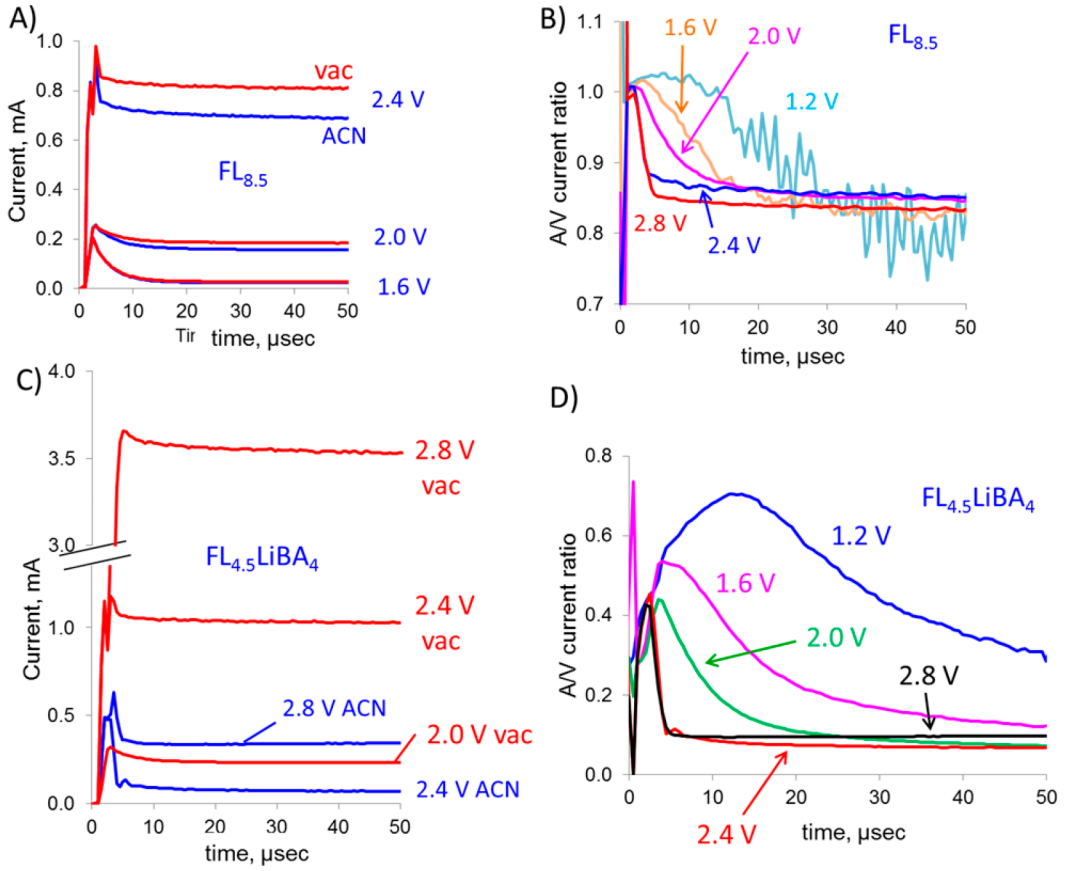

Figure 6. (A) Current transients for bias steps from V = 0 to +1.6, +2.0 and +2.4 V for an $FL_{8.5}$ junction in a vacuum and ACN; (B) ratio of current in ACN over that in a vacuum for $FL_{8.5}$ on a 50 μs time scale; (C) current vs time pulses for $FL_{4.5}/LiBA_4$ in a vacuum (red curves) and ACN (blue curves) for V = +2.0, +2.4 and +2.8 V; (D) current ratios in ACN over vacuum (A/V) for $FL_{4.5}$ $LiBA_4$ junction on a 50 μs time scale.

yield and standard deviations of J are provided in Table S3 for all junction types in a vacuum and ACN vapor, and representative JV curves with error bars are provided in SI section 7 and Figure S7. Briefly, the yield defined as percentage of nonshorted devices was 92 to 100% for at least three different samples (chips), and the relative standard deviation of J for the lower row of four junctions on each sample ranged from 8 to 15%. As shown in the ln J vs V plot of Figure 4D, there is a significant increase in the open circuit potential (OCP, where J = 0) in the presence of ACN vapor for $FL_{4.5}/LiBA_4$, from OCP = +47 ± 3 (N = 5) to +213 ± 6 mV (N = 5), whereas the J = 0 point for $FL_{8.5}$ is −4 ± 1 mV (N = 5) in a vacuum or −21 ± 2 mV (N = 5) in ACN vapor. The similarity of the JV responses for $FL_{8.5}$ and $FL_{4.5}/LiBA_4$ in a vacuum is expected, because both FL and BA have large HOMO−LUMO gaps (Table S1) and d > 5 nm.[28,35] ACN vapor alone would not be expected to significantly affect a tunneling mechanism, consistent with the small ACN effect on $FL_{8.5}$. The large effect of ACN for the Li^+ on current and OCP containing bilayer was investigated further with electrochemical impedance spectroscopy and bias pulse experiments.

Electrochemical impedance spectroscopy (EIS) with a 50 mV modulation amplitude (DC bias = 0) measured in vacuum was used to determine device capacitance as a function of frequency using techniques similar to those reported for large area MJs with Ag/alkane/eGain structures.[36] The goodness of fit (SI, Table S4) was excellent ($<10^{-4}$), and the Nyquist and Bode plots (Figure S9) indicate a typical Randles circuit accurately models the eC-based MJs, with the real component of the capacitance shown in Figure 5A. For $FL_{8.5}$ junctions, the capacitance decreases gradually with frequency from ∼1.0 to 0.7 $\mu F/cm^2$, similar to that reported previously for thinner aromatic MJs.[37] Based on a parallel plate capacitor model, the dielectric constant for $FL_{8.5}$ is 8.7 ± 0.5 at 10 kHz, which is also consistent with ∼5 nm thick aromatic MJs reported previously. ACN vapor increases the capacitance for $FL_{8.5}$ by ∼20%. The capacitance for $FL_{4.5}/LiBA_4$ in a vacuum is also close to 1.0 $\mu F/cm^2$ in a vacuum, but greatly increases to ∼5 $\mu F/cm^2$ in ACN vapor. The capacitance decreases slowly with frequency up to 100 kHz, then more rapidly to ∼1.5 $\mu F/cm^2$ at the instrumental upper limit of 1 MHz. The apparent dielectric constant for $FL_{4.5}/LiBA_4$ at 10 kHz is 46 ± 2 for a parallel plate, too high for aromatic molecules and a possible indication of Li^+ motion. The effect of temperature on the $FL_{4.5}/LiBA_4$ capacitance is shown in Figure 5B for both vacuum and ACN atmospheres, with a ∼20% decrease in a vacuum at 10 kHz at 200 K. However, the high frequency roll-off in ACN shifts to lower frequency between 300 and 200 K, indicating that the capacitance is thermally activated at high frequency. The large difference between the $FL_{4.5}/LiBA_4$ behavior in ACN and the other MJs is also apparent in the Nyquist and Bode plots shown in SI, Figure S9.

The decrease in capacitance for $FL_{4.5}/LiBA_4$ above 100 kHz in ACN indicates the presence of rapid device changes on a ∼10 μs time scale, so the current responses of $FL_{8.5}$ and $FL_{4.5}/LiBA_4$ MJs were monitored for bias pulses lasting 50 μs. Figure 6A shows the current transients resulting from bias steps from zero to +1.6, + 2.0 and +2.4 V applied to the same $FL_{8.5}$ MJ,

DOI: 10.1021/jacs.8b03228
J. Am. Chem. Soc. 2018, 140, 7239−7247

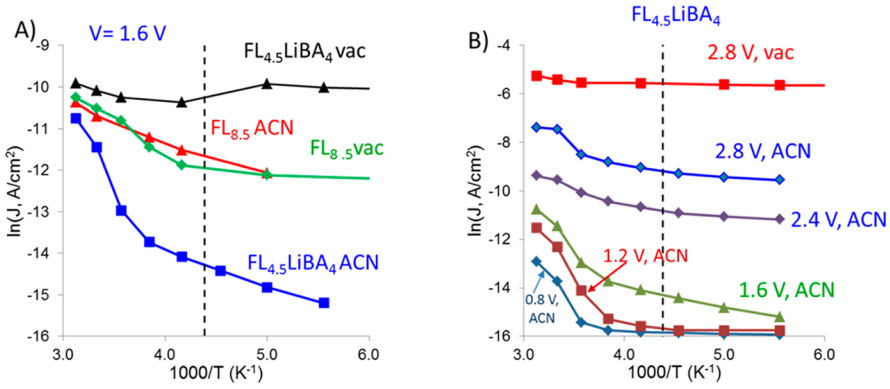

Figure 7. (A) Arrhenius plots (ln J vs 1000/T, K^{-1}) for $FL_{8.5}$ junction in a vacuum (green curve) and that for $FL_{4.5}LiBA_4$ in a vacuum (black curve), ACN (blue curves) at 1.6 V and (B) Arrhenius plots FL_4 $LiBA_{4.5}$ in a vacuum and ACN at +0.8, +1.2, +1.6, +2.4 and +2.8 V, as indicated. Vertical dashed lines are the melting point of ACN

initially in a vacuum, then after ACN vapor exposure. As expected from the JV results of Figure 4C, the current observed in ACN vapor (blue curves) is lower than that in a vacuum (red curves) by 10−20%, obvious trends for 5−50 μs after the bias step. However, the ratio of the current in ACN to that in a vacuum (A/V ratio) plotted in Figure 6B reveals a bias-dependent transition from an initial ratio of 1.0 to 0.85 after 50 μs. The final A/V ratio is weakly dependent on bias voltage, but the transition becomes monotonically faster with increasing bias. Because there are no intentional ions or water vapor in the $FL_{8.5}$ device, a likely origin for the decreased current in ACN vapor is reorientation of polar ACN molecules in the applied electric field, which reduces the electric field across the molecular layer by partial screening. The rate of reorientation of ACN is expected to increase with higher field as observed in Figure 6B, and occurs in <5 to 20 μs in the nominally solid-state junction interior.

The pulse experiment on a $FL_{4.5}/LiBA_4$ junction is shown in Figure 6C, for the same MJs in a vacuum, followed by ACN exposure. Consistent with the JV curves of Figure 4C, ACN greatly reduces the observed current, by >90% at 50 μs and V = 2.8 V. Although the A/V current ratio does not start at 1.0 like those for $FL_{8.5}$, it does exhibit a bias-dependent transition from ∼0.3 to ∼0.09. The distinct shape of the $FL_{4.5}/LiBA_4$ combined with the very different initial and final currents compared to $FL_{8.5}$ indicate that Li^+ has added significantly to the polarization effect evident in Figure 6B. If the differences are due to additional electrode screening by Li^+ motion, then ionic transport in solid-state molecular junctions can be quite fast. For comparison, the conductivity of Na^+ in Nasicon ($Na_3Zr_2Si_2PO_{12}$) is 0.002 S/cm at 25 °C,[38] and is typical of many solid-state ionic conductors. The predicted transit time for Na^+ across a 10 nm of Nasicon with a Na^+ number density of 1.2×10^{18} cm^{-3} under a 2 V bias is 0.6 μs.

The effect of temperature on JV responses of $FL_{8.5}$ and $FL_{4.5}/LiBA_4$ is shown in SI (Figure S13), and summarized in the Arrhenius plots of Figure 7 and in Table 1. The $FL_{8.5}$ Arrhenius plots are very similar in a vacuum or ACN atmosphere, with the apparent slopes near room temperature consistent with the 100−140 meV reported previously for thinner FL junctions (≤5 nm).[35] For $FL_{4.5}/LiBA_4$ in a vacuum, the Arrhenius slopes are weakly dependent on bias and similar to those observed for $FL_{8.5}$ alone. However, the ACN atmosphere strongly affects the temperature dependence for $FL_{4.5}/LiBA_4$, with slopes above 400 meV for $V \leq$ +1.6 V. In addition, the difference in current

Table 1. Arrhenius Slopes (meV) near 300 K for Five Bias Voltages

	T range, K	0.8 V	1.2 V	1.6 V	2.4 V	2.8 V
$FL_{8.5}$ (vacuum)	260−320	32	172	132	108	80
$FL_{8.5}$ (ACN)	260−320	72	73	87	80	70
$FL_{4.5}/LiBA_4$ (vacuum)	280−320	89	63	61	65	53
$FL_{4.5}/LiBA_4$ (ACN)	260−320	463	477	408	128	210

density between vacuum and ACN atmospheres for $FL_{4.5}/LiBA_4$ increases at lower temperature, from a factor of ∼2 at 320 K to a factor of ∼200 at 180 K.

An example of the consequences of ion motion on electronic behavior is shown in Figure 8A for starting with $FL_{4.5}/LiBA_4$ in ACN vapor. The black curve is the first voltammetric scan at 1000 V/s, after which scans were repeated with 12.5 ms between scans. As noted earlier, the initial JV response is nearly symmetric, with the rectification ratio (RR), defined as the absolute value of $J(+1\ V)/J(-1\ V)$, equal to 1.3 ± 0.1. With additional scanning, the RR increases to 6.6 ± 0.2 on the fourth scan and 18 ± 1 on the seventh scan. As shown in Figure 8B, fluorene junctions lacking Li^+ remain symmetric with repeated scanning, but Li^+ containing MJs show dynamic asymmetry in either vacuum or ACN vapor. When scanning was stopped at V = 0 for 10 min, the JV curve returned to its initial state and was indistinguishable from that of the first scan. The entire cycle of increasing RR with repeated scanning was repeatable at least four times.

Finally, the possibility of Li^+ intercalation into one or both eC electrodes was considered by using a different carbon material on the substrate electrode. Pyrolyzed photoresist film (PPF) is similar to glassy carbon and totally sp^2 hybridized (Scheme S3),[32,39] whereas eC is amorphous and ∼30% sp^3 hybridized. As shown in SI section 9 (Figures S10−12), PPF/$FL_{4.5}/LiBA_4$/eC/Au devices showed similar behavior to those containing two eC electrodes, with similar large effects of either air or ACN exposure. The transient responses and EIS results were also similar to those shown in Figures 5 and 6, although with less pronounced effects and poorer reproducibility. Though neither PPF nor eC is expected to efficiently intercalate Li^+, the similarity of their responses is evidence against intercalation playing a significant role in the behavior of $FL_{4.5}/LiBA_4$ devices.

DOI: 10.1021/jacs.8b03228
J. Am. Chem. Soc. 2018, 140, 7239−7247

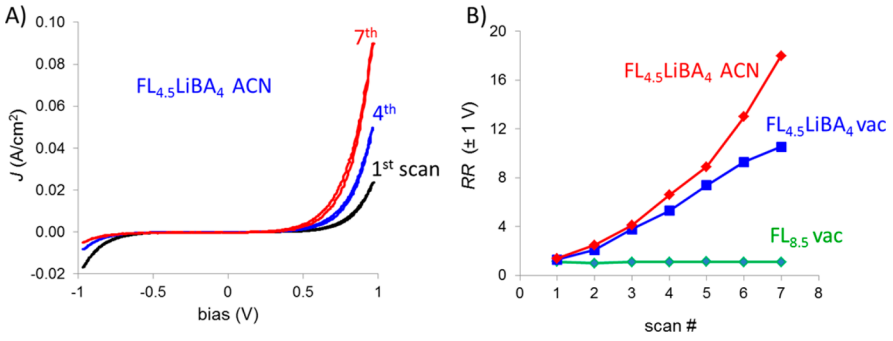

Figure 8. (A) *JV* responses of plots $FL_{4.5}LiBA_{4.5}$ junction in ACN at repetitive scans (1st, 4th, 7th); (B) rectification ratio (RR) at ±1 V for $FL_{8.5}$ in a vacuum (green curve), $FL_{4.5}LiBA_{4.5}$ junction in a vacuum (blue curve), ACN (red curve).

DISCUSSION

The effects of water vapor on organic electronic devices are well-known, and have been discussed in the context of molecular junctions in several recent reports. They include drastic changes in rectification,[4,5] redox activity[21,40] and device degradation.[11,13,27] For the current devices, Figure 3 shows that atmospheric water can significantly and often irreversibly modify *JV* behavior, making interpretation difficult. Water molecules can solvate ions, undergo redox reactions to generate H_2/OH^- and/or O_2/H^+, or ionize to form H^+ and OH^-, and any of these effects could significantly alter junction behavior and stability. As water can undergo redox reactions when the bias exceeds ∼1.2 V and the MJs start to deviate from vacuum behavior when the bias exceeds ∼1 V (Figure 3B), water redox is the likely source of hysteresis in air, rather than CO_2 or other atmospheric gases. The vacuum and ACN vapor conditions used for all results in Figures 4−7 resulted in reliable *JV* behavior, and avoided redox reactions so that the effects of solvation and possible ion motion could be investigated without complications from H_2O. We showed previously that ACN vapor can permeate the top contact, presumably through defects and grain boundaries in the Au and eC layers.[22,31] Starting with FL_5, the *JV* response of Figure 4A exhibits a small reduction (∼10%) in magnitude in the presence of ACN, and both vacuum and ACN responses are stable with time and repeated scanning. The $LiBA_{4.5}$ MJs have a similar *JV* response to FL_5 in either vacuum or ACN, but do exhibit hysteresis in ACN. As noted above, significant differences between FL and LiBA devices were not expected when $d \leq 5$ nm,[34] hence the investigation of the thicker $FL_{8.5}$ and $FL_{4.5}LiBA_4$ MJs.

The addition of ACN vapor to an 8.5 nm FL junction in a vacuum causes a small decrease in current (Figure 4C), which is more apparent in the pulse experiments of Figure 6B. The currents in a vacuum and ACN are equal at $t = 0$, but the ACN current decreases by 15% after 50 μs, with the decrease becoming more rapid as the pulse voltage is increased. In addition, the impedance results indicate a ∼20% higher capacitance in ACN vapor than in a vacuum, with a correspondingly higher apparent dielectric constant. These results are all consistent with reorientation of the polar ACN molecule in the applied electric field, which adds to the dielectric constant of the MJ regardless of whether FL or $FL_{4.5}LiBA_4$ is present. The effect of ACN is conceptually similar to the well-known "solvent reorientation" that occurs at electrode surfaces in electrochemistry, which contributes to the observed electrode capacitance even in the absence of mobile ions.[41,42] Although the MJ is nominally a solid-state device, the molecules are rotationally disordered and not crystalline, so there is apparently sufficient internal void space for ACN molecules to reorient and possibly translate in the applied electric field.

The *JV* response when both LiBA and ACN vapor are present is clearly distinct from $FL_{8.5}$ junctions or the same $FL_{4.5}LiBA_4$ device in a vacuum. For both the *JV* (Figure 4C) and pulse (6D) responses, the current is decreased by ∼85% when the $FL_{4.5}LiBA_4$ in a vacuum is exposed to ACN vapor. The OCP which is present in $FL_{4.5}LiBA_4$ junctions in either vacuum (OCP = +47 ± 3 mV) or ACN (OCP = +214 ± 6 mV), but much smaller and negative in FL junctions is an important indicator of the origin of the large effect of ACN vapor on Li^+ containing MJs. A positive OCP indicates charge separation within the molecular layers, with the FL side more positive than the LiBA side. If Li^+ ions were mobile in the unbiased $FL_{4.5}LiBA_4$ device, there would be a concentration gradient at the FL/LiBA interface which would promote Li^+ motion into the FL layer. The carboxylate anions are immobile, so charge separation would occur and the FL layer would become electrostatically charged positive at open circuit. This effect is obviously absent in an MJ containing only fluorene, but could occur with LiBA present, and ACN vapor should increase the extent of Li^+ mobility by solvating both Li^+ and carboxylate anions. This effect is well-known in solutions, both as "junction potentials" between two dissimilar ionic solutions and "membrane potentials" across ion selective electrodes or biological membranes. Li^+ is expected to cross the FL/LiBA interface until the electrostatic potential across the interface is large enough to impede further Li^+ motion, shown schematically in Figure 8B.

The capacitance results of Figure 5 provide additional clear evidence for both solvent reorganization and ionic effects in the solid-state MJs. For $FL_{8.5}$ in a vacuum, the capacitance is nearly constant with frequency, with a ∼20% decrease from 10^2 to 10^6 Hz. Addition of ACN vapor to the $FL_{8.5}$ MJs in a vacuum results in a ∼40% increase in capacitance over the entire frequency range, implying that ACN reorientation occurs on a microsecond time scale. ACN vapor increases the capacitance of $FL_{4.5}LiBA_4$ junctions by a factor of 5 up to ∼100 kHz (Figure 5A), with a temperature dependent roll-off between 0.1 and 1 MHz (Figure 5B). The capacitance results are consistent with $Li(ACN)_x^+$ motion on a several microsecond time scale, resulting in an increase in the effective dielectric constant. The temperature dependence shown in Figure 7 and Table 1 further support the distinct nature of the $FL_{4.5}LiBA_4$ device in ACN vapor. The Arrhenius slopes of 50−140 meV in the absence of mobile Li^+ are typical for those of electronic conduction in aromatic molecules,[33,35,43] and occur for all cases except

DOI: 10.1021/jacs.8b03228
J. Am. Chem. Soc. 2018, 140, 7239−7247

$FL_{4.5}LiBA_4$ in ACN. The much higher apparent activation energies for $FL_{4.5}LiBA_4$ with ACN present of >400 meV are consistent with the 130[44] to 500 meV[45,46] reported for Li^+ motion in solid electrolytes such as polyethylene glycol.

The pulse response for $FL_{4.5}LiBA_4$ in ACN compared to that in a vacuum shown in Figure 6D does not start with an A/V ratio of ~1.0 as was the case for $FL_{8.5}$. Apparently, the conditions leading to the large reduction in current by ACN vapor are present either at $t = 0$ or arise within less than 5 μs after $t = 0$. For $V \geq 2.4$ V, the A/V ratio rapidly decreases from ~0.3 to ~0.1 with a response time close to the instrumental limit. For lower bias pulses, the current in ACN exhibits a transient response that becomes slower as the bias is decreased. This transient is much too slow for purely electronic changes in the conductance, and is also much slower than the estimated parallel-plate RC time constant of ~1 μs. Contributions to the transient A/V ratio are likely the changes in internal electric field from ionic screening shown schematically in Figure 1C,D, and the ionic current associated with ion motion. A rough estimate of the ionic current yields ~1 mA over 25 μs, based on Li^+ coverage of 4×10^{-10} mol/cm^2 and MJ area of 6.2×10^{-4} cm^2. This ionic current is analogous to the double layer charging current of an electrode in electrolyte solution, and in a molecular junction should result in a transition from the typical energy level schematic of Figure 1B to partial electrode screening in Figure 1C. As predicted in Figure 1D, screening is predicted to have a large effect on the internal electric field, with a possibly significant decrease in the field in the device interior and an increase near one or both electrode interfaces.

Some possible electric field and potential profiles that explain the experimental results are illustrated in Figure 9. For the separated FL and LiBA layers shown in 9A, the electric field is expected to be flat between the electrodes at $V = 0$, with ions absent in FL and evenly distributed in LiBA. When the FL and LiBA layers are in contact, the Li^+ concentration gradient causes Li^+ transfer into the FL layer until it is counteracted by the immobile COO^- groups left behind. The result is the positive OCP observed in the resting junction, with the larger OCP in ACN vapor presumably due to greater partitioning of the $Li(ACN)_x^+$ ion into the FL layer compared to in a vacuum.

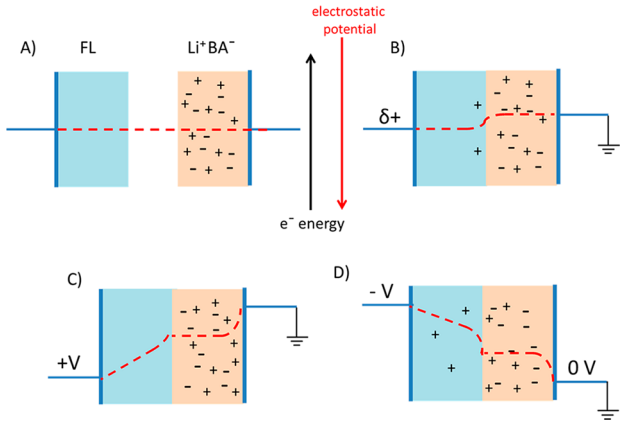

Figure 9. (A) Schematic illustration of an internal electric field when $FL_{4.5}$ and $LiBA_4$ are separated, (B) when $FL_{4.5}$ and $LiBA_4$ layers are in contact, (C) potential profile of $FL_{4.5\ nm}LiBA_{4\ nm}$ junction under positive bias and (D) under negative bias. The "+" and "−" symbols in the diagram represent Li^+, and COO^- ion, respectively, and the arrows indicate the vertical axes of electrostatic potential and electron energy.

Application of a positive bias should drive Li^+ ions into the LiBA layer and build up the Li^+ density near the right electrode of Figure 9C. The potential profile in Figure 9C is expected to be asymmetric and differ from that shown in Figure 1C because the anionic groups in $FL_{4.5}LiBA_4$ are not mobile. The electric field across the LiBA layer is reduced by electrode screening compared to that predicted for a linear potential profile (as in Figure 1B), and the lower field in the molecular layer is likely the primary reason for the reduced current in the $FL_{4.5}LiBA_4$ device in ACN vapor. The extent of entry of Li^+ into the FL layer under negative bias is currently unknown, but Figure 9D shows that a reduction in electric field in the LiBA layer can also occur for negative bias. Because transport across more than 5 nm is consistent with a sequence of tunneling steps[28,35] and/or a hopping mechanism,[47−50] a low electric field in either layer should significantly reduce transport through the molecular junction.

As noted previously for organic electronic devices with $d \geq$ 100 nm, ionic screening can be very useful for reducing the "injection barrier" between electrodes and internal molecular energy levels,[8,13,15,51] shown schematically for molecular junctions in Figure 1C. This effect is not expected for FL or LiBA because their frontier orbitals are too far from the electrode Fermi level for resonant injection and the main effect of ions is reduction of the electric field in the molecular layer, analogous to that shown in Figure 1D. Ionic screening may be involved in "bipolar injection" into $Ru^{2+}(bpy)_3$ centers, leading to light emission in both "thick" (>100 nm) films[11,13] and MJs (<10 nm).[27] The current results indicate that ion motion and screening are possible in 8.5 nm MJs, and that the time scale for reorientation of polar molecules and Li^+ motion can be in the micro- to millisecond range at ambient temperatures. In terms of practicality, it should be possible to seal ACN vapor in MJs using readily available water barriers such as Parylene, which greatly extended the lifetime of light emitting MJs similar to those studied here.[27] Given the importance of the internal potential profile and electric field to the electronic behavior of molecular junctions, we anticipate that ionic screening will enable unusual electronic phenomena such as resonant transport in addition to the commonly studied off-resonant tunneling, and possibly increased performance of light emitting molecular devices[27] and "on chip" energy storage.[22]

■ ASSOCIATED CONTENT

Supporting Information

The Supporting Information is available free of charge on the ACS Publications website at DOI: 10.1021/jacs.8b03228.

Fabrication of molecular junctions, electrochemical grafting, thickness measurements by AFM "scratching", elemental analysis by XPS study, impedance measurements, temperature dependent JV measurements, JV responses on PPF, device yield and statistics and DFT calculated HOMO and LUMO energies (PDF)

■ AUTHOR INFORMATION

Corresponding Author

*richard.mccreery@ualberta.ca

ORCID

Prakash Chandra Mondal: 0000-0002-9415-5147

Richard L. McCreery: 0000-0002-1320-4331

Author Contributions

†Contributed equally to the research.

DOI: 10.1021/jacs.8b03228
J. Am. Chem. Soc. 2018, 140, 7239−7247

Notes

The authors declare no competing financial interest.

■ ACKNOWLEDGMENTS

This work was supported by the University of Alberta, the National Research Council of Canada, the Natural Sciences and Engineering Research Council, and Alberta Innovates. The authors thank Dr. Scott R. Smith, Prof J.-C. Lacroix and Dr. Quyen van Nguyen for valuable scientific discussions and Bryan Szeto for assistance with Labview programming.

■ REFERENCES

(1) Kozicki, M. N.; Mitkova, M.; Park, M.; Balakrishnan, M.; Gopalan, C. *Superlattices Microstruct.* **2003**, *34*, 459−465.
(2) Kumar, R.; Pillai, R. G.; Pekas, N.; Wu, Y.; McCreery, R. L. *J. Am. Chem. Soc.* **2012**, *134*, 14869−14876.
(3) Waser, R.; Dittmann, R.; Staikov, G.; Szot, K. *Adv. Mater.* **2009**, *21*, 2632−2663.
(4) Capozzi, B.; Xia, J.; Adak, O.; Dell, E. J.; Liu, Z.-F.; Taylor, J. C.; Neaton, J. B.; Campos, L. M.; Venkataraman, L. *Nat. Nanotechnol.* **2015**, *10*, 522−527.
(5) Atesci, H.; Kaliginedi, V.; Celis Gil, J. A.; Ozawa, H.; Thijssen, J. M.; Broekmann, P.; Haga, M.-a.; van der Molen, S. J. *Nat. Nanotechnol.* **2018**, *13*, 117−121.
(6) Zhao, W.; Liu, C.-Y.; Wang, Q.; White, J. M.; Bard, A. J. *Chem. Mater.* **2005**, *17*, 6403−6406.
(7) Liu, C.-Y.; Bard, A. J. *J. Am. Chem. Soc.* **2002**, *124*, 4190−4191.
(8) Bernards, D. A.; Flores-Torres, S.; Abruna, H. D.; Malliaras, G. G. *Science* **2006**, *313*, 1416−1419.
(9) Waser, R.; Aono, M. *Nat. Mater.* **2007**, *6*, 833−840.
(10) Szot, K.; Speier, W.; Bihlmayer, G.; Waser, R. *Nat. Mater.* **2006**, *5*, 312−320.
(11) Kalyuzhny, G.; Buda, M.; McNeill, J.; Barbara, P.; Bard, A. J. *J. Am. Chem. Soc.* **2003**, *125*, 6272−6283.
(12) Buda, M.; Kalyuzhny, G.; Bard, A. J. *J. Am. Chem. Soc.* **2002**, *124*, 6090−6098.
(13) Gao, F. G.; Bard, A. J. *J. Am. Chem. Soc.* **2000**, *122*, 7426−7427.
(14) de Mello, J. C.; Tessler, N.; Graham, S. C.; Li, X.; Holmes, A. B.; Friend, R. H. *Synth. Met.* **1997**, *85*, 1277−1278.
(15) de Mello, J. C.; Tessler, N.; Graham, S. C.; Friend, R. H. *Phys. Rev. B: Condens. Matter Mater. Phys.* **1998**, *57*, 12951−12963.
(16) Kaake, L. G.; Zou, Y.; Panzer, M. J.; Frisbie, C. D.; Zhu, X. Y. *J. Am. Chem. Soc.* **2007**, *129*, 7824−7830.
(17) Panzer, M. J.; Frisbie, C. D. *J. Am. Chem. Soc.* **2007**, *129*, 6599−6607.
(18) Yang, J. J.; Pickett, M. D.; Li, X.; Ohlberg, D.; Stewart, D.; Williams, R. S. *Nat. Nanotechnol.* **2008**, *3*, 429−433.
(19) Strukov, D. B.; Williams, R. S. *Appl. Phys. A: Mater. Sci. Process.* **2009**, *94*, 515−519.
(20) Strachan, J. P.; Pickett, M. D.; Yang, J. J.; Aloni, S.; Kilcoyne, A. L. D.; Medeiros-Ribeiro, G.; Williams, R. S. *Adv. Mater.* **2010**, *22*, 3573−3577.
(21) Wu, J.; McCreery, R. L. *J. Electrochem. Soc.* **2009**, *156*, P29−P37.
(22) James, D. D.; Bayat, A.; Smith, S. R.; Lacroix, J.-C.; McCreery, R. L. *Nanoscale Horizons* **2018**, *3*, 45−52.
(23) Fatemi, V.; Kamenetska, M.; Neaton, J. B.; Venkataraman, L. *Nano Lett.* **2011**, *11*, 1988−1992.
(24) Vezzoli, A.; Grace, I.; Brooke, C.; Wang, K.; Lambert, C. J.; Xu, B.; Nichols, R. J.; Higgins, S. J. *Nanoscale* **2015**, *7*, 18949−18955.
(25) Milan, D. C.; Al-Owaedi, O. A.; Oerthel, M.-C.; Marqués-González, S.; Brooke, R. J.; Bryce, M. R.; Cea, P.; Ferrer, J.; Higgins, S. J.; Lambert, C. J.; Low, P. J.; Manrique, D. Z.; Martin, S.; Nichols, R. J.; Schwarzacher, W.; García-Suárez, V. M. *J. Phys. Chem. C* **2016**, *120*, 15666−15674.
(26) Carlotti, M.; Degen, M.; Zhang, Y.; Chiechi, R. C. *J. Phys. Chem. C* **2016**, *120*, 20437−20445.
(27) Tefashe, U. M.; Nguyen, Q. V.; Lafolet, F.; Lacroix, J.-C.; McCreery, R. L. *J. Am. Chem. Soc.* **2017**, *139*, 7436−7439.
(28) Morteza Najarian, A.; Bayat, A.; McCreery, R. L. *J. Am. Chem. Soc.* **2018**, *140*, 1900−1909.
(29) Van Dyck, C.; Ratner, M. A. *J. Phys. Chem. C* **2017**, *121*, 3013−3024.
(30) Van Dyck, C.; Ratner, M. A. *Nano Lett.* **2015**, *15*, 1577−1584.
(31) Das, B. C.; Szeto, B.; James, D. D.; Wu, Y.; McCreery, R. L. *J. Electrochem. Soc.* **2014**, *161*, H831−H838.
(32) Morteza Najarian, A.; Szeto, B.; Tefashe, U. M.; McCreery, R. L. *ACS Nano* **2016**, *10*, 8918−8928.
(33) Bayat, A.; Lacroix, J.-C.; McCreery, R. L. *J. Am. Chem. Soc.* **2016**, *138*, 12287−12296.
(34) Sayed, S. Y.; Fereiro, J. A.; Yan, H.; McCreery, R. L.; Bergren, A. J. *Proc. Natl. Acad. Sci. U. S. A.* **2012**, *109*, 11498−11503.
(35) Morteza Najarian, A.; McCreery, R. L. *ACS Nano* **2017**, *11*, 3542−3552.
(36) Sangeeth, C. S. S.; Wan, A.; Nijhuis, C. A. *J. Am. Chem. Soc.* **2014**, *136*, 11134−11144.
(37) Bergren, A. J.; McCreery, R. L.; Stoyanov, S. R.; Gusarov, S.; Kovalenko, A. *J. Phys. Chem. C* **2010**, *114*, 15806−15815.
(38) Horwat, D.; Billard, A. *Ionics* **2005**, *11*, 120−125.
(39) Ranganathan, S.; McCreery, R. L.; Majji, S. M.; Madou, M. *J. Electrochem. Soc.* **2000**, *147*, 277−282.
(40) Bonifas, A. P.; McCreery, R. L. *Anal. Chem.* **2012**, *84*, 2459−2465.
(41) Shaw, S. K.; Lagutchev, A.; Dlott, D. D.; Gewirth, A. A. *J. Phys. Chem. C* **2009**, *113*, 2417−2424.
(42) Hou, Y.; Aoki, K. J.; Chen, J.; Nishiumi, T. *J. Phys. Chem. C* **2014**, *118*, 10153−10158.
(43) Yan, H.; Bergren, A. J.; McCreery, R.; Della Rocca, M. L.; Martin, P.; Lafarge, P.; Lacroix, J. C. *Proc. Natl. Acad. Sci. U. S. A.* **2013**, *110*, 5326−5330.
(44) Devaux, D.; Villaluenga, I.; Bhatt, M.; Shah, D.; Chen, X. C.; Thelen, J. L.; DeSimone, J. M.; Balsara, N. P. *Solid State Ionics* **2017**, *310*, 71−80.
(45) Polu, A. R.; Kim, D. K.; Rhee, H.-W. *Ionics* **2015**, *21*, 2771−2780.
(46) Vélez, J. F.; Aparicio, M.; Mosa, J. *J. Phys. Chem. C* **2016**, *120*, 22852−22864.
(47) Taherinia, D.; Smith, C. E.; Ghosh, S.; Odoh, S. O.; Balhorn, L.; Gagliardi, L.; Cramer, C. J.; Frisbie, C. D. *ACS Nano* **2016**, *10*, 4372−4383.
(48) Smith, C. E.; Odoh, S. O.; Ghosh, S.; Gagliardi, L.; Cramer, C. J.; Frisbie, C. D. *J. Am. Chem. Soc.* **2015**, *137*, 15732−15741.
(49) Luo, L.; Balhorn, L.; Vlaisavljevich, B.; Ma, D.; Gagliardi, L.; Frisbie, C. D. *J. Phys. Chem. C* **2014**, *118*, 26485−26497.
(50) Choi, S. H.; Kim, B.; Frisbie, C. D. *Science* **2008**, *320*, 1482−1486.
(51) deMello, J. C.; Tessler, N.; Graham, S. C.; Friend, R. H. *Phys. Rev. B: Condens. Matter Mater. Phys.* **1998**, *57*, 12951−12963.

DOI: 10.1021/jacs.8b03228
J. Am. Chem. Soc. 2018, 140, 7239−7247